ADVANCED FUNCTIONAL MATERIALS
www.afm-journal.de

www.MaterialsViews.com

Spinel $ZnMn_2O_4$ Nanocrystal-Anchored 3D Hierarchical Carbon Aerogel Hybrids as Anode Materials for Lithium Ion Batteries

Longwei Yin, Zhiwei Zhang,* Zhaoqiang Li, Fengbin Hao, Qun Li, Chengxiang Wang, Runhua Fan, and Yongxin Qi*

To improve the electrochemical performance of spinel $ZnMn_2O_4$, i.e., its limited specific capacity, cycling performance, and rate properties, owing to its inherent poor electrical conductivity and large volume changes during lithiation and delithiation processes, spinel $ZnMn_2O_4$ nanocrystals are anchored into a three dimensional (3D) porous carbon aerogel (CA) through a facile solution immersion chemical route. The designed 3D spinel $ZnMn_2O_4$/CA hybrids display the advantages of both spinel $ZnMn_2O_4$ and porous CA: enormous interfacial surface area, connected 3D framework, abundant porosity and high electron transport properties of CA, and electrochemical properties of nanostructured spinel $ZnMn_2O_4$ oxide materials. The synthesized novel $ZnMn_2O_4$/CA hybrids display a significantly improved electrochemical performance, with a high reversible specific capacity, and high-rate capability, as well as an excellent cycling performance, superior to that of previously reported $ZnMn_2O_4$-based materials. After 50 cycles, the 50%$ZnMn_2O_4$/CA hybrid displays a reversible capacity of 833 mAh g^{-1} at a current density of 100 mAg^{-1}, much higher than the theoretical capacity of 784 mAh g^{-1} for pure spinel $ZnMn_2O_4$ materials, corresponding to a Coulombic efficiency of 99.9%. The greatly improved cycle stability, specific capacity, and high rate performance of the $ZnMn_2O_4$/CA hybrids can be attributed to the synergistic interaction between spinel-structured $ZnMn_2O_4$ nanoparticles and the 3D interconnected porous CA matrix.

1. Introduction

Recently, metal oxides with high theoretical capacity are attracting much attention to improve the reversible capacity of anode materials for lithium ion batteries (LIBs). Much attention is paid to two types of oxide systems, one type of oxides (Sn, In and Zn based oxides) can react with Li to form alloyed metal phase during lithiation and delithiation process. For example, SnO_2 oxide can react with Li to form $Li_{4.4}Sn$ alloy, the main drawback is that the capacity may be greatly reduced due to a large volume change during the lithiation and delithiation process.[1–3] For another type of oxide, there will form Li_2O and nanocrystalline metal nanoparticles through redox reaction during the lithiation and delithiation process. This type of oxide mainly includes transition metal oxides based on Mn, Fe, Co, Ni, Cu, etc.,[4–6] displaying no free interstitial sites within their crystallographic structure to host lithium and not forming alloy with lithium. However, they can react reversibly with lithium according to a process termed conversion reaction: $M_xO_y + 2ye^- + 2yLi^+ = xM + yLi_2O$. The theoretical capacity offered by these reactions depends on the oxidation state of the 3d metals existed in the voltage range of interest. Among the transition metal oxides, Co_3O_4 displays excelement elctrochemical performance as anode materials for LIBs.[5,7] Taking into consideration of the toxicity and high cost of Co, inexpensive and environment friendly electrode materials such as Fe- and Mn based oxides may be more popular and promising.

It is interesting to note that many two binary oxides with spinel structure display good electrochemical performance. AB_2O_4 spinel (or spinel-like) structured oxides containing two TMs (A and B), with A having an oxidation state of +2 and B of +3, are attracting much attention as anode materials for LIBs.[8–12] Spinel AMn_2O_4 (A represents Co, Ni, and Zn) series have been extensively investigated as anode materials for LIBs. The $CoMn_2O_4$ powders only exhibit a capacity of 515 mAh g^{-2} with retention of about 64% at a current of 69 mAg^{-2} after 50 cycles. Recently, Lou et al. reported that double shelled $CoMn_2O_4$ hollow microcubes can achieve a capacity of 624 mAh g^{-2} with a retention of about 75.5% at a current of 200 mAg^{-2} after 50 cycles.[10] Shen reported a reversible capacity of 512 mAh g^{-1} at a current density of 200 mAg^{-1} for $CoMn_2O_4$ hollow samples.[11,12] The electrochemical tests showed that the $CoMn_2O_4$ products show a coulombic efficiency of 98% after 100 cycles.

L. W. Yin, Z. W. Zhang, Z. Li, F. Hao, Q. Li, C. Wang, R. Fan, Y. Qi
Key Laboratory for Liquid-Solid Structural Evolution and Processing of Materials
Ministry of Education
School of Materials Science and Engineering
Shandong University
Jinan 250061, PR China
Tel: +86 531 88396970
Fax: +86 531 88396970
E-mail: yinlw@sdu.edu.cn; 339238247@qq.com

DOI: 10.1002/adfm.201400108

Among the Mn based spinel structured anodes, $ZnMn_2O_4$ is particularly interesting with many advantages, such as environmental friendliness, low cost, and much lower operating voltage in comparison with the Co- or Fe- based oxides.[13–15] More importantly, spinel structured $ZnMn_2O_4$ has a low charge-discahrge potential of 0.5 and 1.2 V, so that battery using $ZnMn_2O_4$ as an anode material has a high output potential to increase the current density of LIBs. This compound has a normal spinel structure with the bivalent Zn^{2+} occupying the tetrahedral sites and the trivalent Mn^{3+} occupying the octahedral sites in the spinel structure, which is isostructural to the spinel Co_3O_4. Interestingly, it can store Li^+ through not only the conversion reaction (1), (2), (3), but also the alloying reaction between Zn and Li in reaction (4), leading to a high theoretical capacity of 784 mAh g^{-1}.[16]

$$ZnMn_2O_4 + 8Li^+ + 8e^- \rightarrow Zn + 2Mn + 4Li_2O \quad (1)$$

$$2Mn + 2Li_2O \rightarrow 2MnO + 4Li^+ + 4e^- \quad (2)$$

$$Zn + Li_2O \rightarrow ZnO + 2Li^+ + 2e^- \quad (3)$$

$$Zn + Li^+ + e^- \rightarrow LiZn \quad (4)$$

$ZnMn_2O_4$ displays many advantages as anode materials for LIBs, maintaining a reversible capacity of 626 mAh g^{-1} after 50 cycles.[17,18] However, its specific capacity, cycling performance and rate properties are still limited owing to its inherent poor electrical conductivity and large volume changes resulted form the lithiation and delithiation for $ZnMn_2O_4$ material. Thus, it is highly desirable to develop novel hybrids based on spinel $ZnMn_2O_4$ materials as high performance anodes for LIBs. However, there is relatively little progress on nanohybrid anodes based on the nanostructured spinel $ZnMn_2O_4$ materials. As is known, the introduction of conductive carbon layers is one of the most common approaches to enhance the electrical conductivity of electrode materials.[19]

Due to its higher specific capacity and more negative redox potential than most metal oxides, mesoporours carbon with 3D and continuous conductive network structure may be a good candidate to make hybrid with spinel nanostructured $ZnMn_2O_4$ as anode materials for LIBs. Carbon aerogel (CA) is a special class of porous material with a high specific surface area, abundantly high micro- and mesoporosity, and 3D well-connected through pore structure and enormous interfacial surface area. These structural features favor CA for applications involving heterogeneous reactions at solid-liquid interfaces such as electrodes and catalysts.[20–23] For desirable 3D porous CA materials as anodes, the large surface areas can provide abundant active sites for the interfacial events, high porosities and through pore structure can enable fast mass transfer of the liquid species to access the active sites, and 3D well-connected network can offer continuous charge transport passageways.

In this article, we designed 3D interconnected spinel $ZnMn_2O_4$/CA hybrids via a low-temperature solvothermal two-step route. Both advantages of spinel $ZnMn_2O_4$ and 3D interconnected CA are combined according to the following three different concepts: the high surface area and abundant porosity of CA, the nanostructured spinel oxide materials for their electrochemical properties, and the high electron transport properties of CA materials. The electrochemical performance demonstrated that the developed $ZnMn_2O_4$/CA hybrids display considerably outstanding higher Coulombic efficiency, better capacity retention ability and rate capability compared with pure $ZnMn_2O_4$ and CA materials. It is noted that the electrochemical performance of the 3D interconnected mesoporous $ZnMn_2O_4$/OMC hybrid is evidently better than the previous pure and hybrids of related spinel $ZnMn_2O_4$ materials. This novel hybrid provides a new route to design and synthesize future electrode materials for high performance LIBs applications.

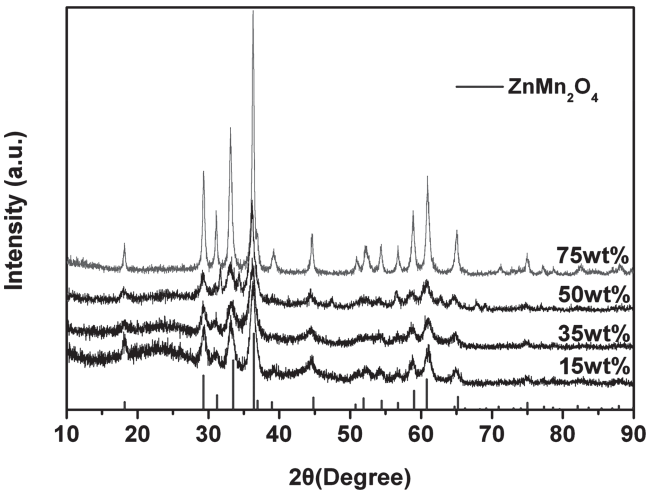

Figure 1. (a) X-ray diffraction (XRD) patterns of $ZnMn_2O_4$/CA hybrids.

2. Results and Discussion

Figure 1 shows the XRD patterns of the $ZnMn_2O_4$/CA nanohybrids with different $ZnMn_2O_4$ loading contents. A typical tetragonal spinel structure with a space group of $I4_1/amd$ and lattice constants of a = 5.7204 Å, c = 9.2450 Å (JCPDS No.24–1133) for $ZnMn_2O_4$ can be determined. With the increase of $ZnMn_2O_4$ content in the $ZnMn_2O_4$/CA nanohybrids, the amorphous peaks related to CA matrix get weaker and almost disappear as the content is up to 75%, while the peak intensity of the crystalline $ZnMn_2O_4$ becomes stronger. This indicates that the synthesized products are composed of $ZnMn_2O_4$ and amorphous CA, without any other impurity phase contained.

The Brunauer–Emmett–Teller (BET) specific surface area and porous characteristics of the $ZnMn_2O_4$/CA hybrid samples were investigated by nitrogen adsorption–desorption isotherms. The nitrogen adsorption–desorption isotherms and pore size distribution of $ZnMn_2O_4$/CA hybrid samples with different incorporated $ZnMn_2O_4$ contents are given in **Figure 2**a,b. All $ZnMn_2O_4$/CA samples exhibit typical type IV isotherms with a H_1 hysteresis loop with a similar curve to that of pure CA sample, indicating the incorporation of $ZnMn_2O_4$ does not basically destroy the porous structure of CA matrix. The textural parameters of $ZnMn_2O_4$/CA hybrid samples including

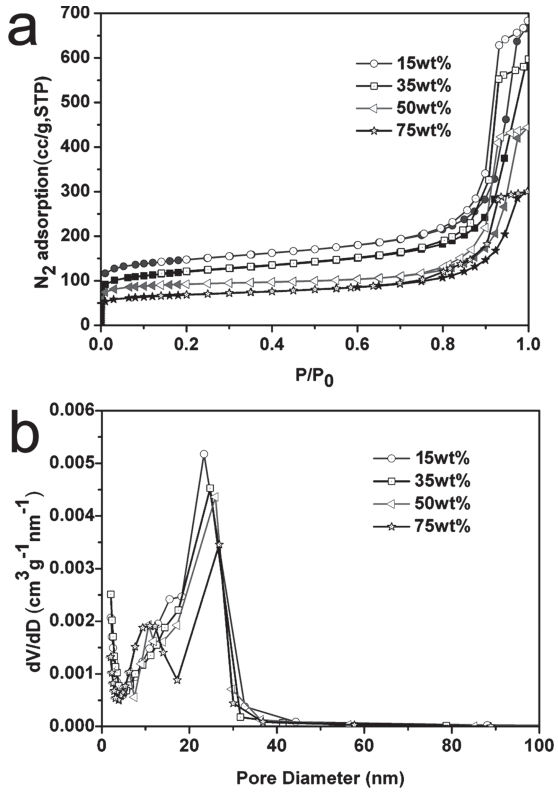

Figure 2. (a,b) N_2 adsorption–desorption isotherms and pore size distribution of $ZnMn_2O_4$/CA hybrid samples with different $ZnMn_2O_4$ contents.

BET surface area, porous volume, and pore size distribution are summarized in **Table 1**. With the content of $ZnMn_2O_4$ incorporated in CA matrix increasing, the surface area, pore size, the volume of pores and micropores gradually decrease. For the 50% and 75% $ZnMn_2O_4$/CA hybrid samples, the average pore size is 11.3 and 10.1 nm, and the micropore volume is reduced to be only 0.08 and 0.05 cm^3g^{-1}, respectively. This is because the incorporation of $ZnMn_2O_4$ induces the pore blocking and the density increase of the hybrids.

The Raman spectra of $ZnMn_2O_4$/CA hybrid and pure CA samples are illustrated in **Figure 3**. Two peaks are observed at 1321 cm^{-1} (D band) and 1588 cm^{-1} (G band) for pure CA sample, are attributed to the Raman active *E*2g mode of the graphitic carbon lattice vibration, and the *A*1g mode of disordered carbon originating from some kind of imperfection.[24] For the graphitization degree of the carbon materials, it is generally evaluated according to the ratio of the intensity of the D band (I_D) to G (I_g) band (I_D/I_G). The I_D is higher than I_G in the spectrum of pure CA sample, indicating that CA sample

Table 1. Textural parameters of $ZnMn_2O_4$/CA hybrids.

Sample	Surface area [m^2g^{-1}]	Pore size [nm]	Pore volume [cm^3g^{-1}]	Micropore volume [cm^3g^{-1}]
15wt%	554	15.2	1.08	0.19
35wt%	461	13.9	1.01	0.14
50wt%	382	11.3	0.88	0.08
75wt%	252	10.1	0.62	0.05

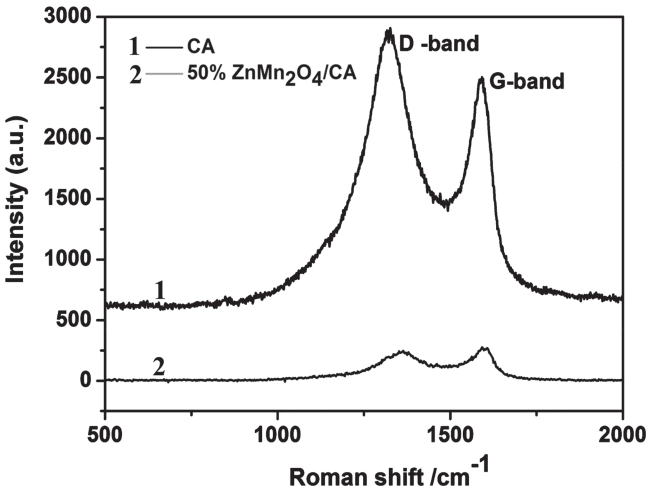

Figure 3. Raman spectra for 50%$ZnMn_2O_4$/CA nanohybrids and pure CA.

has a structure with a fraction of graphitic cluster dispersed in disordered carbon.[25] After combination of $ZnMn_2O_4$ with three-dimensional interconnected CA matrix, a microstructure evolution takes place for the $ZnMn_2O_4$/CA hybrids. The D band shifts from the 1321 to 1360 cm^{-1}, while the G band shifts from 1588 to 1599 cm^{-1}. Furthermore, the intensity of I_D decreases and the intensity of I_G increases relatively, so the ratio for the I_D to I_G (I_D/I_G) decreases compared with that of pure CA sample, indicating that the $ZnMn_2O_4$/CA hybrids are more disordered.[26]

The microstructures and surface morphologies of $ZnMn_2O_4$/CA hybrids with different contents of $ZnMn_2O_4$ incorporated are characterized by field emission scaning electron microscopy (FESEM) , as shown in **Figure 4**. The FESEM image of 15% $ZnMn_2O_4$/CA hybrid can be demonstrated in Figure 4a. As revealed, the 15%$ZnMn_2O_4$/CA hybrids maintain the 3D interconnected framework of CA matrices, with CA nanoparticles of an average size of 20–30 nm connected each other to form the 3D interconnected porous hierarchical structures. (Please see transmission electron microscopy (TEM) images for pure CA in Figure S1 in the Supporting Information). Maybe because of the low content and small size of the spinel structured $ZnMn_2O_4$ nanoparticles in the $ZnMn_2O_4$/CA hybrids, it is not easy to identify the $ZnMn_2O_4$ nanoparticular phase according to FESEM image of 15%$ZnMn_2O_4$/CA hybrids. The size and distribution, phase structure of $ZnMn_2O_4$ nanocrystals in the hybrids can be further revealed by the following TEM microstructures of 15%$ZnMn_2O_4$/CA hybrid shown below.

With the content of incorporated $ZnMn_2O_4$ nanoparticles increasing, $ZnMn_2O_4$ nanoparticles occupy more porous sites of CA matrix, and the nanocrystalline $ZnMn_2O_4$ nanoparticles tend to aggregate to form larger $ZnMn_2O_4$ nanoparticles around some porous sites of CA matrix, as shown in Figure 4b. The size of the aggregated $ZnMn_2O_4$ nanoparticles on surface of the 35%$ZnMn_2O_4$/CA hybrid is about 30 nm. Figure 4c depicts a typical FESEM image of 50%$ZnMn_2O_4$/CA nanohybrid. As the incorporated content of $ZnMn_2O_4$ is up to 50%, most of the pores are inhabited by the $ZnMn_2O_4$ nanoparticles, and more and more $ZnMn_2O_4$ nanoparticles tend to aggregate on the surface of CA matrix to form relatively larger $ZnMn_2O_4$

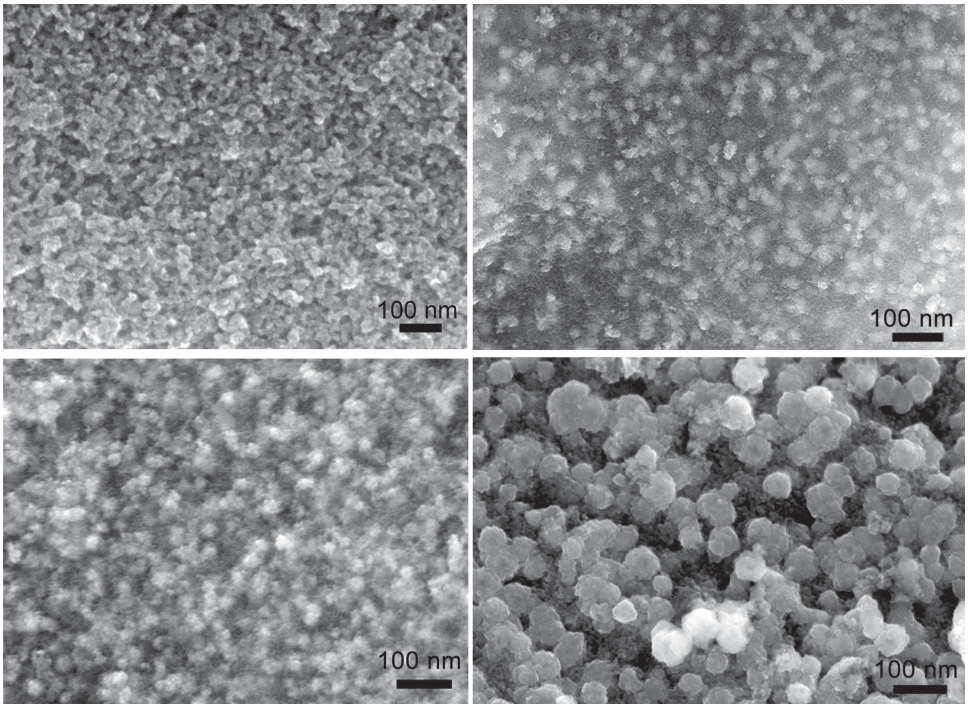

Figure 4. (a–d) FESEM images of $ZnMn_2O_4$/CA hybrids with different incorporating contents of 15, 35, 50, 75% of $ZnMn_2O_4$.

nanocrystals with a size of about 40 nm. As the content of incorporated $ZnMn_2O_4$ nanocrystals is up to 75%, the nanocrystals aggregate to form large particles with an average diameter of 100–120 nm (Figure 4d).

Figure 5 depicts a typical EDS spectrum (Figure 5b) for the hybrids (Figure 5a) and elemental mapping of the hybrid samples (Figure 5c–f), clearly showing that the synthesized hybrid products are composed of O, Zn, Mn and C elements with a homogeneous distribution for all the elements. It is suggested the $ZnMn_2O_4$ nanoparticles are homogenously distributed among the CA matrices.

To further reveal the microstructural nature of the $ZnMn_2O_4$/CA hybrids, TEM is utilized to describe the size, morphology, distribution, and the phase structure of $ZnMn_2O_4$/CA hybrids. **Figure 6**a,b gives low magnification TEM images of 15%$ZnMn_2O_4$/CA hybrid. $ZnMn_2O_4$ nanoparticles about several nanometers with dark contrast homogeneously distribute among the 3D porous connected CA matrix. A typical electron diffraction pattern in Figure 6c suggests the polycrystalline nature of the spinel structured $ZnMn_2O_4$ nanopartciles. The diffraction rings in Figure 6c correspond well to (103), (211), (220), and (224) planes of tetragonal sipnel $ZnMn_2O_4$. A typical

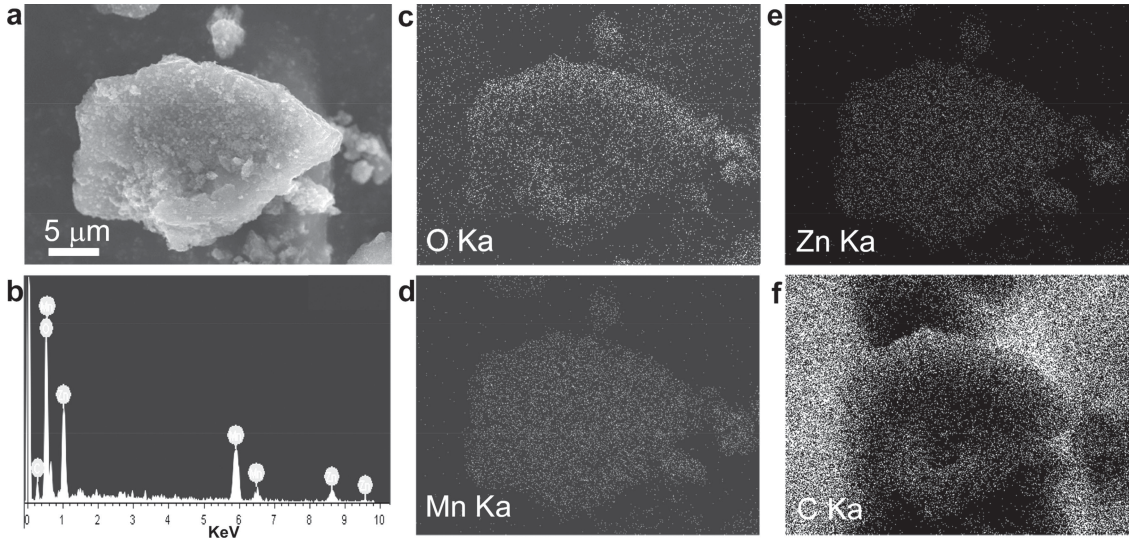

Figure 5. (a) A low magnification FESEM image. (b) A typical EDS spectrum. (c–f) O, Zn, Mn, C elemental mapping of $ZnMn_2O_4$/CA nanohybrids.

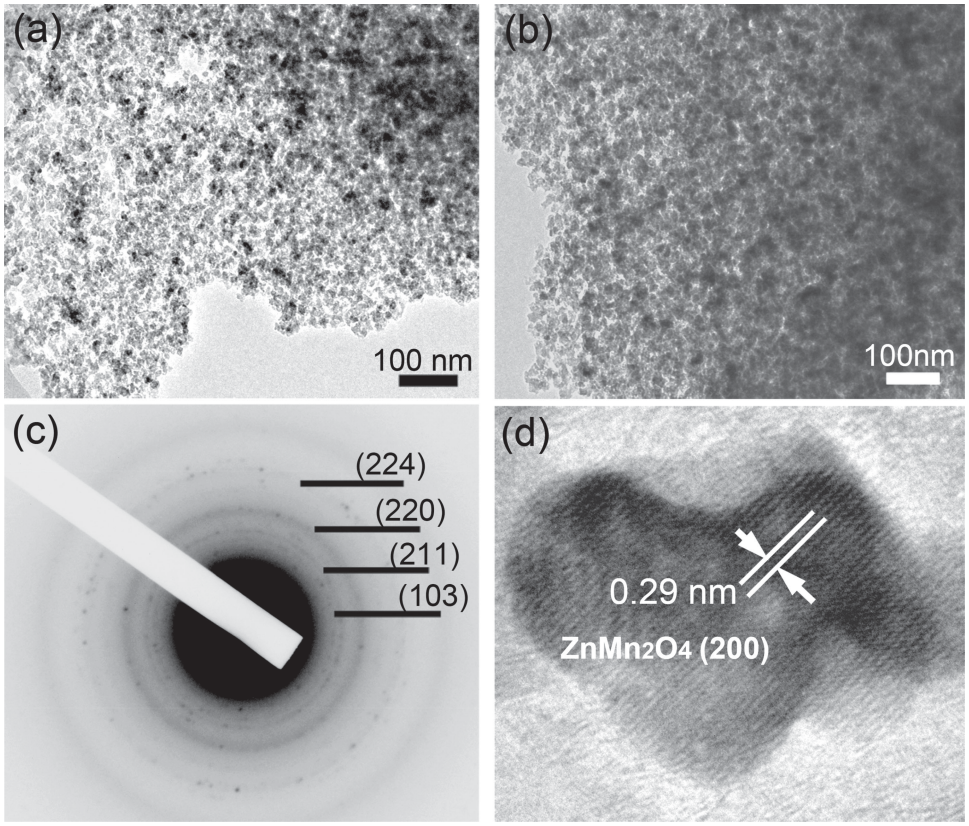

Figure 6. (a,b) Low magnification TEM images of 15%$ZnMn_2O_4$/CA hybrid. (c) A typical electron diffraction pattern. The diffraction rings correspond well to (103), (211), (220), and (224) planes of tetragonal sipnel $ZnMn_2O_4$. (d) The marked 0.29 nm in a HRTEM lattice image of a single $ZnMn_2O_4$ nanparticle matches well with d-spacing of (200) plane of spinel structured $ZnMn_2O_4$.

HRTEM lattice image of a single $ZnMn_2O_4$ nanparticle is depicted in Figure 6d. The marked 0.29 nm matches well with d-spacing of (200) plane of spinel structured $ZnMn_2O_4$.

As the content of $ZnMn_2O_4$ incorporated increases, almost most of the microporous and a large amount of mesoporous sites are occupied, the nanoparticles aggregate to form large sized $ZnMn_2O_4$ nanoparticles. As indicated by low- and high-magnification TEM images of 35%$ZnMn_2O_4$/CA hybrid in **Figure 7**a,b, $ZnMn_2O_4$ nanoparticles tend to accumulate around the mesoporous sites to form large sized nanoparticles of about 40 nm, displaying a connected rod like shape in correspondence with the 3D interconnected porous CA structure. The HRTEM lattice image in Figure 7c is taken along the [201] zone axis, the marked d-spacing of 0.31 nm corresponds well to d-spacing of $(1\bar{1}2)$ and $(11\bar{2})$ planes of spinel tetragonal $ZnMn_2O_4$. The corresponding ED pattern is given in Figure 7d.

Figure 8a–f show cyclic voltammetric (CV) curves of the first three cycles for CA, $ZnMn_2O_4$/CA hybrids with incorporated contents of 15, 35, 50, 75% for $ZnMn_2O_4$, pure $ZnMn_2O_4$ samples at a scan rate of 0.1 mV s^{-1} between 0.01–3.0 V. The cyclic voltammetry (CV) curves of 50%$ZnMn_2O_4$/CA hybrid is given in Figure 8d. There exists two obvious reduction peaks at 1.22 V and 0.70 V in the first cycle, which are believed to be correspondent with the reduction process of Mn^{3+} to Mn^{2+} and the formation of a solid electrolyte interface (SEI). The reduction peaks at 1.22 V and 0.70 V disappear in the following subsequent cycle, indicating that there will not form Mn^{3+} in the reverse reaction process. This is then followed by another reduction peak at 0.13 V that corresponds to (i) the reduction of Mn^{2+} and Zn^{2+} to nanodomains of Mn^0 and Zn^0 embedded in Li_2O matrix, and then (ii) the alloying reaction of Zn with Li to form ZnLi. It should be noted that with the content of $ZnMn_2O_4$ incorporated increasing, the reduction peaks tend to shift to left position with low potential (Figure 8b–e), closing to that of pure $ZnMn_2O_4$ in Figure 8f. In the oxidation process, the oxidation peak at 1.30 V[27,28] is closely associated with the reactions of $Mn \rightarrow Mn^{2+}$ and $Zn \rightarrow Zn^{2+}$.[17] For the whole lithiation and delithiation process of $ZnMn_2O_4$/CA hybrid anode electrode, the reactions can be summarized as following. Firstly, the $ZnMn_2O_4$ is reduced to ZnLi, Mn and Li_2O, and then reverse reaction of ZnLi, Mn, Li_2O and ZnO, MnO, Li^+.[18]

$$ZnMn_2O_4 + 9Li^+ + 9e^- \rightarrow ZnLi + 2Mn + 4Li_2O$$
$$ZnLi + 2Mn + 3Li_2O \leftrightarrow ZnO + 2MnO + 7Li^+ + 7e^-$$

The initial five charge-discharge curves between 0.01 and 3.0 V at the current of 100 mAg^{-1} for CA, $ZnMn_2O_4$/CA hybrids with incorporated contents of 15, 35, 50, 75% of $ZnMn_2O_4$, and pure $ZnMn_2O_4$ samples are illustrated in **Figure 9**a–f, respectively. The initial five discharge and charge curves of 50%$ZnMn_2O_4$/CA nanohybrid is depicted in Figure 9d. The initial discharge capacity of 50%$ZnMn_2O_4$/CA hybrid, CA and

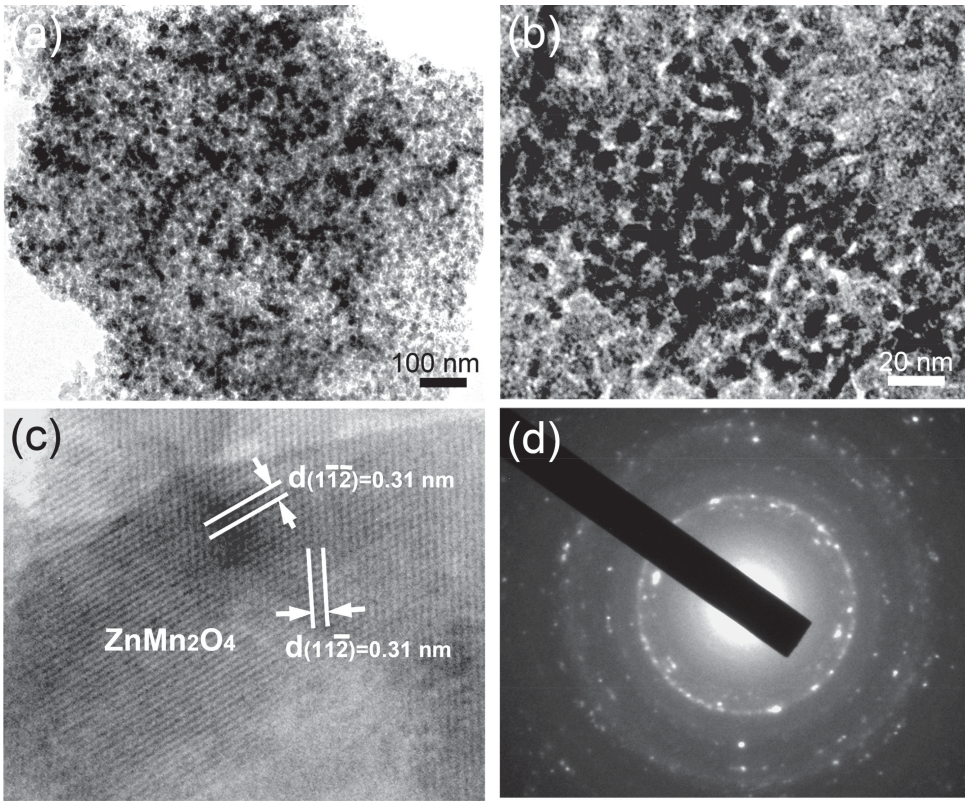

Figure 7. (a,b) Low and high magnification TEM images of 35%$ZnMn_2O_4$/CA hybrid. (c) A HRTEM lattice image taken along [201] zone axis, the marked d-spacing of 0.31 nm corresponds well to d-spacing of $(1\bar{1}\bar{2})$ and $(11\bar{2})$ planes of spinel tetragonal $ZnMn_2O_4$. (d) Electron diffraction pattern.

pure $ZnMn_2O_4$ is 1660, 1463, 1177 mAh g^{-1}, and a charge capacity of 886, 565, 513 mAh g^{-1}, respectively, corresponding to an initial Coulombic efficiency of 53.4, 38.7, 43.6%. At the 5th cycle, the discharge capacity of 50%$ZnMn_2O_4$/CA hybrid, CA and pure $ZnMn_2O_4$ is 791, 450, 417 mAh g^{-1}, displaying a Coulombic efficiency of 95.7, 82.2, 95.2%, respectively. It is shown that it is an effective route to improve the specific capacity and Coulombic efficiency of $ZnMn_2O_4$ via the combination of $ZnMn_2O_4$ and porous CA to form the 3D interconnected porous $ZnMn_2O_4$/CA hybrids. As the content of $ZnMn_2O_4$ is low, the discharge and charge potential plateau are not obvious. (Figure 9b–e) With the content of $ZnMn_2O_4$ incorporated in CA matrix increasing, the discharge potential increases remarkably, and both the discharge and charge potential plateau become obvious.

Figure 10a comparatively illustrates the cycling performance of CA, $ZnMn_2O_4$/CA hybrids and pure $ZnMn_2O_4$ electrodes at a current density of 100 mA g^{-1}. At the 10th cycle, the CA, $ZnMn_2O_4$/CA hybrid and $ZnMn_2O_4$ can retain a reversible capacity value of 420, 745, 667, 729, 568, 371 mAh g^{-1}, respectively. After 10 cycles, the reversible capacity tends to be stable, except for 75%$ZnMn_2O_4$/CA hybrid and pure $ZnMn_2O_4$ samples decreasing rapidly with the cycle time increasing. During the 10 to 50 cycles, the reversible capacity of the $ZnMn_2O_4$/CA hybrids (15, 35, 50%$ZnMn_2O_4$) almost does not decrease, the reversible capacity even increases with the cycling time increasing.

At 50th cycle, the reversible capacity of 15, 35, 50%$ZnMn_2O_4$/CA hybrids can maintain a reversible capacity of 714, 781, 833 mAh g^{-1}, displaying a Coulombic efficiency of 99.5, 99.7, 99.9%, respectively. While for 75% $ZnMn_2O_4$/CA hybrid sample, the reversible capacity decreases rapidly with the cycle time increasing. After 50 cycles, 75%$ZnMn_2O_4$/CA hybrid sample only shows a reversible capacity of 375 mAh g^{-1}, remarkably lower than that of the hybrids with the $ZnMn_2O_4$ incorporated content lower than 50%, only a retention of 22% percentage of initial discharge capacity of 1695 mAh g^{-1}. The pure $ZnMn_2O_4$ and CA sample only shows a reversible capacity of 410 and 270 mAh g^{-1}, respectively. The specific reversible capacity of 833 mAh g^{-1} for 50%$ZnMn_2O_4$/CA hybrid is 2.03 times higher than that of 410 mAh g^{-1} for pure CA sample, and 3.1 times higher than that of 270 mAh g^{-1} for pure $ZnMn_2O_4$ sample.

It is clearly shown that 50%$ZnMn_2O_4$/CA hybrid shows a much higher capacity, better capacity retention of 50.3% of the first discharge capacity (from 1657 to 833 mAh g^{-1}), and more superior cyclability of stabilizing at ~96.2% from the 5th cycle onward, and its reversible capacity even gradually increases. The similar increasing trend of the specific capacity with cycle prolonging was also reported by Huang et al. in the MoO_2/graphene composite.[29]

To investigate the rate capability of $ZnMn_2O_4$/CA hybrid samples, the $ZnMn_2O_4$/CA hybrid anodes were cycled for each ten cycles under an increasing current density of 100, 200,

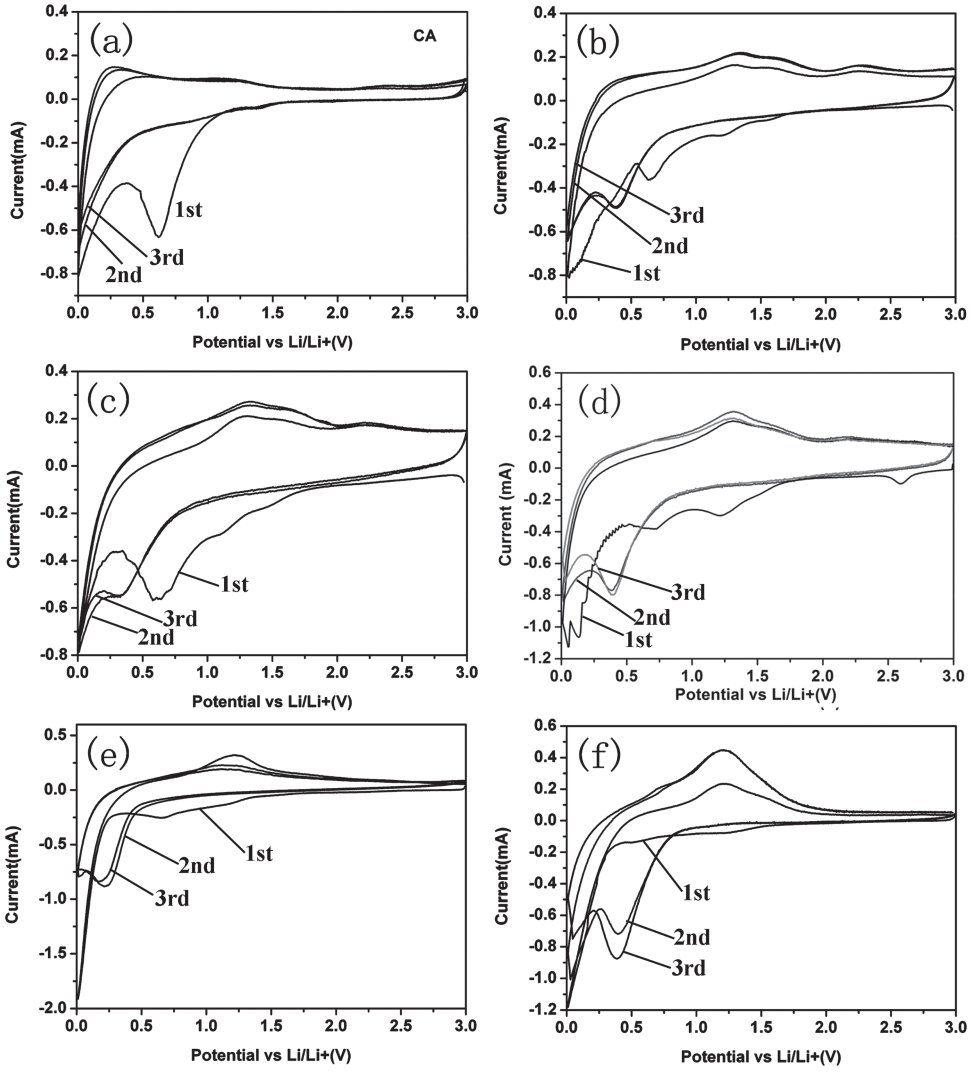

Figure 8. Cyclic voltammetric (CV) curves of the first three cycles for (a) CA, (b–e) $ZnMn_2O_4$/CA hybrids with incorporated contents of 15, 35, 50, 75% for $ZnMn_2O_4$, and (f) pure $ZnMn_2O_4$ samples at a scan rate of 0.1 mV s^{-1} between 0.01–3.0 V.

400, 800, and 1600 mA g^{-1}, as shown in Figure 10b. The discharge capacities gradually decreased with increasing of the current rate. For pure $ZnMn_2O_4$ sample, the pulverizing and cracking effect of $ZnMn_2O_4$ nanoparticles during charge/discharge process results in the capacity decreasing drastically, and the reversible capacity only remains 98 mAh g^{-1} at a high charge rate of 1600 mA g^{-1} after 50 cycles, namely retention of 7.6% of the initial capacity. While for the $ZnMn_2O_4$/CA hybrid samples, with the increasing of current density and cycle times prolonging, they display much outstanding rate performance than that of pure $ZnMn_2O_4$ and CA samples. At a high current density of 1600 mA g^{-1}, 50%$ZnMn_2O_4$/CA hybrid still retains an excellent cyclic performance of ~242 mAh g^{-1} even after 50 cycles, which is approximately about 2.47 times higher than that of pure $ZnMn_2O_4$ and CA (98 mAh g^{-1}). As the current density returns back to 100 mA g^{-1}, the capacity of the 50%$ZnMn_2O_4$/CA hybrid electrode still maintains at 910 mAh g^{-1} after 60 cycles, much better than that of pure $ZnMn_2O_4$ (427 mAh g^{-1}).

The presently reported significantly improved electrochemical performance of high reversible specific capacity, specific capacity and high-rate capability, and excellent cycling performance of $ZnMn_2O_4$/CA hybrid is superior to that of previously reported $ZnMn_2O_4$ based materials. For example, a polymer-pyrolysis route synthesized flower-like tetragonal $ZnMn_2O_4$ superstructures (30–60 nm) can remain a capacity of 626 mAh g^{-1} after 50 cycles.[18] While for nanocrystalline $ZnMn_2O_4$ electrode, it delivered a stable capacity of 569 mAh g^{-1} after 50 cycles cycled at 100 mA g^{-1} between 0.01 and 3.0 V.[14,30] Fabrice's study suggests that $ZnMn_2O_4$ particles of about 5 nm in diameter give a high capacity of 430 mAh g^{-1} when cycled 100 times at C/10.[31] It is shown that the nanoflake-shaped $ZnMn_2O_4$ particle prepared via calcination of an agglomerated Zn–Mn citrate complex precursor, can provide a capacity value of 650 mAh g^{-1} at a current density of 100 mA g^{-1}.[13] Lou et al recently reported that $ZnMn_2O_4$ ball-in-ball hollow microsphere as a high-performance anode for LIBs shows a discharge capacity at around 490 mAh g^{-1} after about

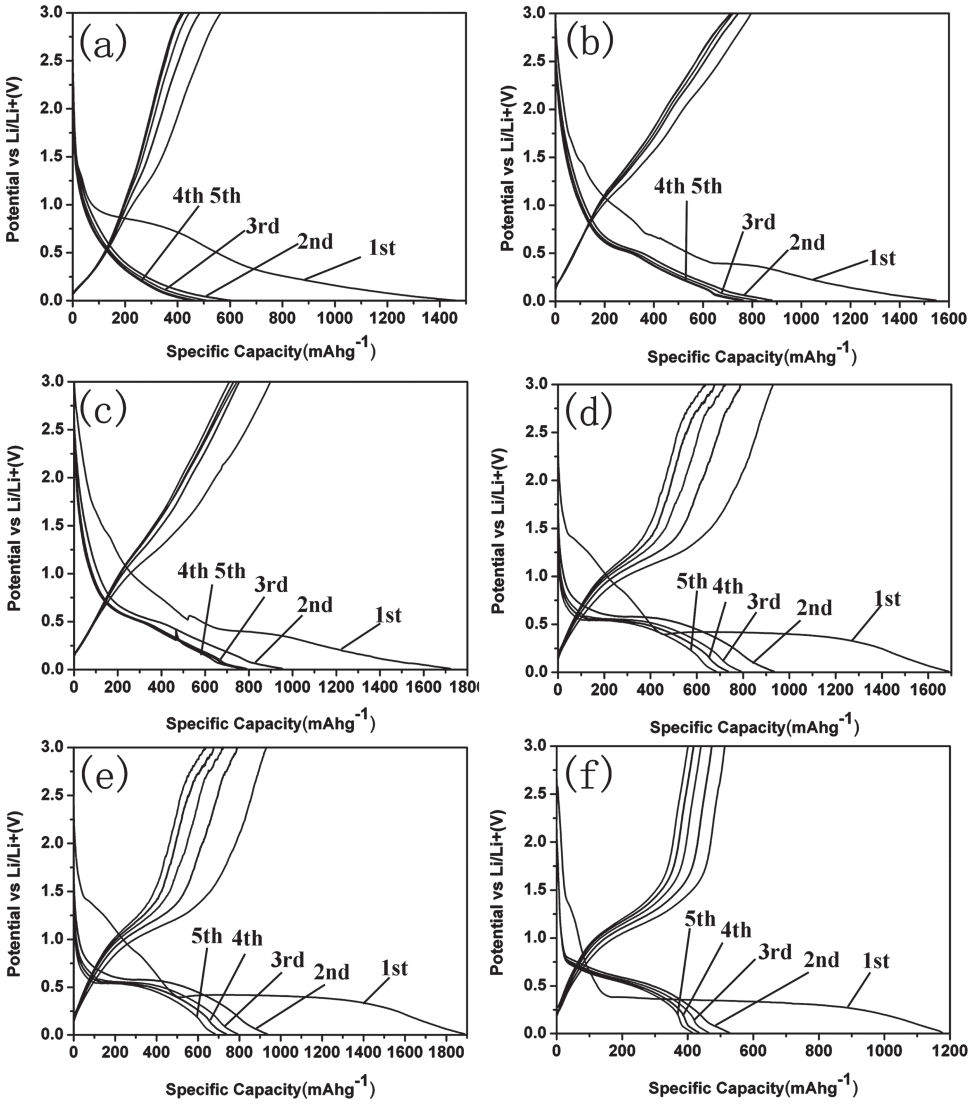

Figure 9. The initial five charge-discharge curves between 0.01 and 3.0 V at the current of 100 mAg^{-1} for (a) CA, (b–e) $ZnMn_2O_4$/CA hybrids with incorporated contents of 15, 35, 50, 75% for $ZnMn_2O_4$, (f) pure $ZnMn_2O_4$ samples.

50 cycles.[24] The loaf-like $ZnMn_2O_4$ nanorods exhibit a reversible capacity of 517 mAh g^{-1} at a current density of 500 mA g^{-1} after 100 cycles.[25] Recently, it is reported that spinel $ZnMn_2O_4$ nanoplate assemblies fabricated via "escape-by-crafty-scheme" strategy shows a slower capacity decay rate and maintains a nearly constant value of about 502 mAh g^{-1} after 30 cycles.[26]

The greatly improved cycle stability, specific capacity and high rate performance of the $ZnMn_2O_4$/CA hybrids can be attributed to the synergistic interaction between spinel structured $ZnMn_2O_4$ nanoparticles and 3D interconnected porous CA matrix. (i) The 3D connected porous CA acts as a mechanical buffer to relax the volume changes of the $ZnMn_2O_4$ nanoparticles generated during Li^+ insertion/extraction, and as a conductive layer to enable the interfacial stabilization of $ZnMn_2O_4$ nanocrystals, and can effectively build up a network to ensure good electrical contact between $ZnMn_2O_4$ nanoparticles and 3D connected porous CA to increase reaction kinetics (**Figure 11**a). (ii) Furthermore, the open porous channels of the 3D connected framework of CA allow sufficient infiltration of electrolyte and provide fast diffusion channels of Li^+. (iii) Spinel structrued $ZnMn_2O_4$ nanoparticles homogeneously distributing in CA appropriately reduce the number of active sites of CA to increase the initial reversible capacity and the capacity retention, improving the initial Coulombic efficiency. (iV) According to EIS analysis (Figure 11b), the $ZnMn_2O_4$/CA nanohybrid electrode possesses lower charge-transfer resistance and faster reaction rate during the Li ion charge-discharge process. The decrease of charge transfer resistance is beneficial for improving the reaction kinetics of the $ZnMn_2O_4$/CA nanohybrid electrode, and hence, enhancing the electrochemical performance of the $ZnMn_2O_4$/CA nanohybrid electrode for LIBs.

It is should be noted that the 50%$ZnMn_2O_4$/CA hybrid displays the mostly improved electrochemical performance of high reversible specific capacity, specific capacity and high-rate capability, and excellent cycling performance compared with

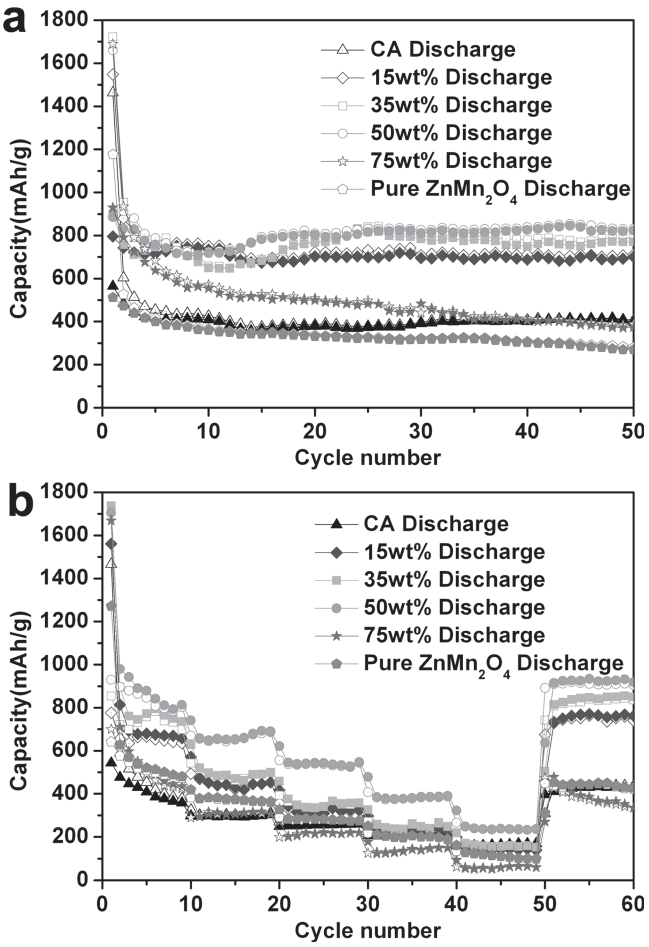

Figure 10. (a) Capacity vs. cycle number curves at the discharge current of 100 mAg^{-1}, and (b) rate capacity curves of $ZnMn_2O_4$/CA hybrids between 0.01 V and 3.0 V.

pure spinel $ZnMn_2O_4$ and CA, and other $ZnMn_2O_4$/CA hybrid materials. As the content of $ZnMn_2O_4$ incorporated is lower than 50%, the specific capacity of the $ZnMn_2O_4$/CA hybrid gradually increases with the content of $ZnMn_2O_4$ increasing. This is attributed to the synergistic intersection between the $ZnMn_2O_4$ and CA, the $ZnMn_2O_4$ nanoparticles are distributed around the porous sites of the CA matrix, and the CA matrix can effectively prevent the aggregation of $ZnMn_2O_4$ nanoparticles. However, as the content of $ZnMn_2O_4$ is higher than 50%, the $ZnMn_2O_4$ nanoparticles aggregate to form large sized $ZnMn_2O_4$ particeles (see FESEM image of 75%$ZnMn_2O_4$/CA hybrid in Figure 4b). The synergistic intersection between the $ZnMn_2O_4$ nanoparticle and CA matrix disappears, resulting in electrochemical performance degradation of the $ZnMn_2O_4$/CA hybrids.

3. Conclusions

The tetragonal spinel $ZnMn_2O_4$ nanocrystals were incorporated into 3D porous interconnected framework of carbon aerogels through a facile solution immersion chemical route. The designed 3D interconnected spinel $ZnMn_2O_4$/CA hybrids are based on both advantages of spinel $ZnMn_2O_4$ and 3D interconnected CA according to the following three different concepts: the high surface area and abundant porosity of CA, the nanostructured spinel oxide materials for their electrochemical properties, and the good electron transport properties of CA materials. The electrochemical performance demonstrated that the developed $ZnMn_2O_4$/CA hybrids display considerably outstanding higher Coulombic efficiency, better capacity retention and rate capability compared with pure $ZnMn_2O_4$ and CA materials. This novel hybrid provides a new route to design and synthesize future electrode materials for high performance LIBs applications.

4. Experimental Section

Preparation of $ZnMn_2O_4$/CA Hybrids: The CA materials were synthesized according to previously reported methods.[32] The $ZnMn_2O_4$/CA hybrids were synthesized as following. Proper content of manganese nitrate and zinc nitrate precursors were added into small of water according to a molar ratio of 2:1, then 0.5 g of CA materials were added to the above solution, the mixture was magnetically stirred for 12 h at room temperature to assure that manganese nitrate and zinc nitrate were fully adsorbed on the surface of CA. The resultant mixtures

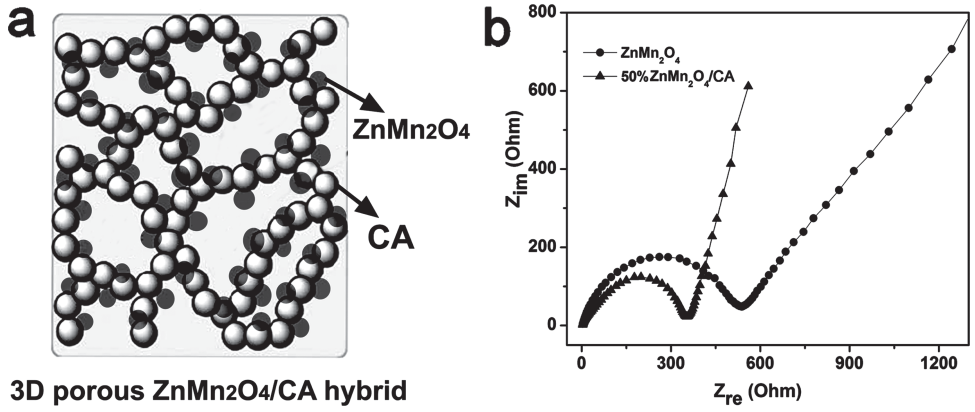

Figure 11. (a) Structural model for 3D porous interconnected $ZnMn_2O_4$/CA hybrid. (b) EIS spectra of 50%$ZnMn_2O_4$/CA hybrid and pure $ZnMn_2O_4$ sample.

were dried at 333 K for 12 h, and subsequently they were calcined at 673 K for 5 h under Ar atmosphere. The $ZnMn_2O_4$/CA hybrids with incorporation contents of 15, 35, 50, 75% $ZnMn_2O_4$ were obtained finally. In order to make a comparison of electrochemical performance between $ZnMn_2O_4$/CA hybrid, pure $ZnMn_2O_4$ and CA materials, pure $ZnMn_2O_4$ was prepared using manganese nitrate and zinc nitrate as precursor reactants.

The phase components and structure of the synthesized products were characterized using Rigaku D/Max-KA diffractometer equipped with Cu *Ka* radiation. The microstructure and chemical components of the products were analyzed using SU-70 field emission scanning electron microscopy (FESEM), high-resolution transmission electron microscopy (HRTEM) of JEM-2100 at an acceleration voltage of 200 kV, respectively. Nitrogen adsorption-desorption isotherms were determined at 77 K using micromeritics ASAP 2020 surface area and porosity analyzer, as reported in our previous work. The surface area measurements were performed according to the Brunauer-Emmett-Teller (BET) method. The pore size distribution was obtained from the desorption branch of isotherm using the corrected form of Kelvin equation by means of the Barrett-Joyner-Halenda (BJH) method. Raman spectra were measured and collected using a 632.8 nm laser with a JY HR800 under ambient conditions, with a laser spot size of about 1 μm.

Electrochemical Measurements: Working electrodes were prepared by mixing 80 wt% of active materials ($ZnMn_2O_4$/CA, pure $ZnMn_2O_4$ and CA), 10 wt% acetylene black (Super-P), and 10 wt% polyvinylidene fluoride binder dissolved in N-methyl-2-pyrrolidinone. The galvanostatic charging/discharging test was the same as previously reported.[33] It was conducted using standard 2032 type coin cells with copper foil as the current collector, lithium foil as reference electrodes and 1.0 M $LiPF_6$ in mixed ethylene carbonate (EC) and diethyl carbonate (DEC) (EC:DEC, 1:1 by volume) as the electrolyte. A cut-off voltage window of 0.01 – 3.0 V was used. The 2032 coin-type cells were assembled in an argon-filled glovebox with less than 1 ppm of oxygen and water, galvanostatically cycled on a LAND CT2001A instrument (Wuhan, China) at room temperature. Cyclic voltammetry (CV) study was conducted using an electrochemical workstation (PARSTAT 2273) between 0.01–3.0 V at a scan rate of 0.1 mV s^{-1}.

Supporting Information

Supporting Information is available from the Wiley Online Library or from the author.

Acknowledgements

We acknowledge support from the National Natural Science Funds for Distinguished Young Scholars (No: 51025211), The National Basic Research Program (No: 2013CB934303), National Nature Science Foundation of China (No: 51272137), the Tai Shan Scholar Foundation of Shandong Province.

Received: January 13, 2014
Revised: February 18, 2014
Published online: April 2, 2014

[1] Y. Idota, T. Kubota, A. Matsufuji, Y. Maekawa, T. Miyasaka, *Science* **1997**, *276*, 1395.
[2] J. O. Besenhard, J. Yang, M. Winter, *J. Power Sources* **1997**, *68*, 87.
[3] A. S. Arico, P. Bruce, B. Scrosati, J. M. Tarascon, W. van Schalkwijk, *Nat. Mater.* **2005**, *4*, 366.
[4] W. Y. Li, L. N. Xu, J. Chen, *Adv. Funct. Mater.* **2005**, *15*, 851.
[5] Y. M. Kang, M. S. Song, J. H. Kim, H. S. Kim, M. S. Park, J. Y. Lee, H. K. Liu, S. X. Dou, *Electroch. Acta* **2005**, *50*, 3667.
[6] H. Li, X. Huang, L. Chen, *Solid State Ionics* **1999**, *123*, 189.
[7] P. Poizot, S. Laruelle, S. Grugeon, L. Dupont, J. M. Tarascon, *Nature* **2000**, *407*, 496.
[8] S. Patoux, L. Daniel, C. Bourbon, H. Lignier, C. Pagano, F. Le Cras, S. Jouanneau, S. Martinet, *J. Power Sources* **2009**, *189*, 344.
[9] N. Sivakumar, S. R. P. Gnanakan, K. Karthikeyan, S. Amaresh, W. S. Yoon, G. J. Park, Y. S. Lee, *J. Alloys Compd.* **2011**, *509*, 7038.
[10] L. Zhou, D. Y. Zhao, X. W. Lou, *Adv. Mater.* **2012**, *6*, 745.
[11] L. J. Wang, B. Liu, S. H. Ran, L. M. Wang, L. N. Gao, F. Y. Qu, D. Chen, G. Z. Shen, *J. Mater. Chem. A* **2013**, *1*, 2139.
[12] B. Liu, J. Zhang, X. F. Wang, G. Chen, D. Chen, C. W. Zhou, G. Z. Shen, *Nano Lett.* **2012**, *12*, 3005.
[13] Y. F. Deng, S. D. Tang, Q. M. Zhang, Z. C. Shi, L. Zhang, S. Zhan, G. H. Chen, *J. Mater. Chem.* **2011**, *21*, 11987.
[14] Y. Y. Yang, Y. Q. Zhao, L. F. Xiao, L. Z. Zhang, *Electrochem. Commun.* **2008**, *10*, 1117.
[15] S. W. Kim, H. W. Lee, P. Muralidharan, D. H. Seo, W. S. Yoon, D. K. Kim, K. Kang, *Nano Res.* **2011**, *4*, 505.
[16] F. M. Courtel, H. Duncan, Y. Abu-Lebdeh, I. J. Davidson, *J. Mater. Chem.* **2011**, *21*, 10206.
[17] D. Pasero, N. Reeves, A. R. West, *J. Power Sources* **2005**, *141*, 156.
[18] L. Xiao, Y. Yang, J. Yin, Q. Li, L. Zhang, *J. Power Sources* **2009**, *194*, 1089.
[19] Z. M. Zheng, Y. L. Cheng, X. B. Yan, R. T. Wang, P. Zhang, *J. Mater. Chem. A* **2014**, *2*, 149.
[20] G. A. M. Reynolds, A. W. P. Fung, Z. H. Wang, M. S. Dresselhaus, R. W. Pekala, *J. Non-Cryst. Solid.* **1995**, *188*, 27.
[21] S. A. Al-Muhtaseb, J. A. Ritter, *Adv. Mater.* **2003**, *15*, 101.
[22] Y. Hanzawa, K. Kaneko, R. W. Pekala, M. S. Dresselhaus, *Langmuir* **1996**, *12*, 6167.
[23] H. C. Chien, W. Y. Cheng, Y. H. Wang, S. Y. Lu, *Adv. Funct. Mater.* **2012**, *22*, 5038.
[24] G. Q. Zhang, L. Yu, H. B. Wu, H. E. Hoster, X. W. (David) Lou, *Adv. Mater.* **2012**, *24*, 4609.
[25] Z. C. Bai, N. Fan, C. H. Sun, Z. C. Ju, C. L Guo, J. Yang, Y. T. Qian, *Nanoscale* **2013**, *5*, 2442.
[26] J. Zhao, F. Q. Wang, P. P. Su, M. R. Li, J. Chen, Q. H. Yang, C. Li, *J. Mater. Chem.* **2012**, *22*, 13328.
[27] K. Zhong, X. Xia, B. Zhang, H. Li, Z. Wang, L. Chen, *J. Power Sources* **2010**, *195*, 3300.
[28] H. Wang, Q. Pan, Y. Cheng, J. Zhao, G. Yin, *Electroch. Acta* **2009**, *54*, 2851.
[29] Y. Sun, X. Hu, W. Luo, Y. Huang, *ACS Nano* **2011**, *5*, 7100.
[30] G. Binotto, D. Larcher, A. S. Prakash, R. H. Urbina, M. S. Hegde, J. M. Tarascon, *Chem. Mater.* **2007**, *19*, 3032.
[31] F. M. Courtel, Y. Abu-Lebdeh, I. J. Davidson, *Electroch. Acta* **2012**, *71*, 123.
[32] Z. Wang, F. Li, N. S. Ergang, A. Stein, *Chem. Mater.* **2006**, *18*, 5543.
[33] N. N. Liu, L. W. Yin, C. X. Wang, L. Y. Zhang, N. Lun, D. Xiang, Y. X. Qi, R. Gao, *Carbon* **2010**, *12*, 3759.